IEEE Access
Multidisciplinary ⋮ Rapid Review ⋮ Open Access Journal

Received 3 May 2024, accepted 9 July 2024, date of publication 12 July 2024, date of current version 23 July 2024.

Digital Object Identifier 10.1109/ACCESS.2024.3427340

RESEARCH ARTICLE

Dual-Band Compact Six-Element Millimeter Wave MIMO Antenna: Design, Characterization, and Its Application for V2V Communication

B. G. PARVEEZ SHARIFF[1], (Graduate Student Member, IEEE), TANWEER ALI[1], (Senior Member, IEEE), PRAVEEN KUMAR[1], SAMEENA PATHAN[2], G. D. GOUTHAM SIMHA[1], PALLAVI R. MANE[1], (Senior Member, IEEE), MOHAMMED GULAM NABI ALSATH[3], (Senior Member, IEEE), AND ALEXANDROS-APOSTOLOS A. BOULOGEORGOS[4], (Senior Member, IEEE)

[1]Department of Electronics and Communication Engineering, Manipal Institute of Technology, Manipal Academy of Higher Education, Manipal 576104, India
[2]Department of Information and Communication Technology, Manipal Institute of Technology, Manipal Academy of Higher Education, Manipal 576104, India
[3]Department of Electronics and Communication Engineering, College of Engineering Guindy, Anna University, Chennai, Tamil Nadu 600025, India
[4]Department of Electrical and Computer Engineering, University of Western Macedonia, 501 00 Kozani, Greece

Corresponding author: Tanweer Ali (tanweer.ali@manipal.edu)

ABSTRACT This article presents a compact six-element multiple-input multiple-output (MIMO) antenna for vehicle-to-vehicle (V2V) communications. The proposed structure is planar, having a dimension of $1.28\lambda_0 \times 2.04\lambda_0$, where λ_0 is the wavelength at 25.5 GHz, resonating in n258 and n260 bands. The antenna is a modified rectangular patch designed to generate TM_{10} and TM_{02} modes, resulting in vertical and horizontal polarization at 25.5 GHz and 38 GHz. The measured bandwidth of the MIMO antenna is 800 MHz at the n258 band, i.e., 25.1-25.9 GHz, and 850 MHz at the n260 band, i.e., 37.75-38.6 GHz. The isolation between the elements is improved by incorporating a novel open-ended decoupling structure. It resulted in an isolation that surpass 20 dB at both bands. The antenna has a broadside radiation pattern with a maximum realized gain of 9 dBi and 7.2 dBi at 25.5 and 38 GHz, respectively. The antenna is validated for various diversity parameters such as envelope correlation coefficient, diversity gain, channel capacity loss, and mean effective gain. Also, the performance of the proposed antenna for V2V communication is analyzed for line-of-sight and non-line-of-sight conditions. The estimated channel capacity, path loss, and link budget for the above-said condition suggest that the antenna is suitable for V2V communications.

INDEX TERMS 5G, decoupling structure, dual-band, link margin, millimeter wave, multiple-input-multiple-output, path loss, vehicle-to-vehicle (V2V).

I. INTRODUCTION

Vehicle automation systems have experienced a drastic advancement over the past decade [1]. With the increased number of sensors and sensor data creating congestion in vehicular communication at sub-6 GHz, the attention is drifting toward the millimeter wave (mmWave) spectrum. The fifth generation (5G) new radio (NR) frequency band ranging from n257-n263 (24.25-71 GHz) is used by various wireless applications, such as cellular, satellite, radar, and vehicular communications [2], because these bands are less prone to atmospheric attenuation. The channel propagation conditions at 28, 38, 60, and 76 GHz are studied for vehicular communications in urban, semi-urban, and highway conditions [3]. For line-of-sight (LOS) communications, the path loss exponent (PLE) is approximately 2, whereas, for non-line-of-sight (NLOS), it becomes even higher [3] at mmWave. However, with the low latency and higher data rate of 3-100 Gb/s, the mmWave spectrum becomes prominent for vehicular communications. Initially, the vehicles are interconnected in vehicle-to-vehicle (V2V) communication to share basic safety information. With the drift to the higher

The associate editor coordinating the review of this manuscript and approving it for publication was Jenny Mahoney.

spectrum and availability of larger bandwidth, the V2V shares a large amount of sensory data for safety purposes, along with non-safety information such as video streaming and high-speed internet access. The throughput for V2V and vehicle-to-everything (V2X) is further improved by adapting multiple-input-multiple-output (MIMO) antenna technology in the physical layer of the Institute of Electrical and Electronics Engineers (IEEE) 802.11p and IEEE 802.11ad protocol [4], [5], [6]. All these developments led to an advanced driver assistance system (ADAS) to achieve robust road safety.

Consequently, numerous MIMO antenna structures are designed to operate at mmWave [7], [8], [9]. However, only a few have demonstrated for vehicular communications. The antennas for V2V communication should be resilient to the shadowing effect, and gain variation must be minimal when mounted on vehicles at different positions [10]. For example, in [11], a planar two-element MIMO with a T-shaped monopole antenna is presented for vehicle-to-vehicle (V2V) communications. The author intends to study the variation in gain and radiation at four different positions on a car. However, the variation in these results is not clearly summarized. The antenna has a parasitic element on either side of the feed line engraved with a complementary-split-ring-resonator (CSRR) to generate resonance at 28, 30, and 37 GHz. It resulted in bandwidth ranging from 27-38 GHz with a maximum gain of 7 dBi. However, the structure dimension is relatively large ($1.12\lambda_0 \times 2.35\lambda_0$ at 28 GHz, where λ_0 stands for the wavelength), and the isolation between elements is unknown. In .) [12], a two-element dipole-shaped MIMO antenna is introduced that operates from 25 to 40 GHz and from 49 to 52 GHz. Bandwidth enhancement is achieved through a J-shaped balun offset feed. Isolation of more than 40 dB is obtained with a T-shaped decoupling structure in the ground plane. However, the structure is compromised with a large dimension of $1.1\lambda_0 \times 1.88\lambda_0$ at 25.5 GHz. In [13], a three-dimensional (3D) eight-element MIMO antenna structure is reported. It has a tapered antenna design, resonating at 2.4 and 26 GHz with a bandwidth ranging from 1.8 to 3.5 GHz and 24 to 28.5 GHz. The structure has an isolation of more than 30 dB at mmWave with a maximum gain of 9 dBi. In [14], a 3D 12-element MIMO antenna is designed to operate at 2.5, 3.5, 5.5, 7.5, and 29 GHz. The structure has four inverted L-shaped stubs to generate multiple resonances. It achieved mmWave bandwidth ranging from 23-31 GHz with a maximum gain of 6.8 dBi. However, the isolation at mmWave is not discussed.

From the aforementioned literature, certain limitations are observed: i) the designs in [11], [13], and [14] have an issue of disconnected ground plane. The MIMO antenna requires a stable and single standard reference voltage point; ii) The designs in [13] and [14] have orthogonal structures, which limits them from scalability and integration with the printed circuit board (PCB) board; iii) The designs in [11], [12], [13], and [14] have large antenna profiles; iv) Another and most important drawback is the lack of analysis of the documented antenna for various V2V and/or V2X communication scenarios.

Motivated by this, this paper introduces a six-element MIMO antenna to address the drawbacks of the above-mentioned antennas. The antenna is planar, simple, and scalable, having a compact dimension of $1.28\lambda_0 \times 2.04\lambda_0$ (where λ_0 is the wavelength at 25.5 GHz). It is designed to resonate at 25.5 GHz (f_0) and 38 GHz (f_1), operating in n258 and n260 NR bands, with bandwidth ranging from 25.1 to 25.9 GHz and 37.75 to 38.6 GHz. The isolation between the elements is achieved with the help of a novel open-ended decoupling structure (DCS), which has contributed to attaining an isolation of more than 20 dB at both bands. The antenna resulted in a gain of 9 dBi and 7.2 dBi, at 25.5 and 38 GHz, respectively. The performance of the antenna in terms of diversity parameter has resulted in an envelope correlation coefficient (ECC) that is less than 0.45, a diversity gain (DG) is more than 9/9.2, a channel capacity loss (CCL) is less than 0.36 b/s/Hz, and a mean effective gain (MEG) is less than -3 dB. The antenna is tested in an anechoic chamber, and the antenna characteristics are validated for channel capacity, path loss, and link budget under LOS and NLOS conditions for various antenna positions for V2V communication scenarios. The technical contribution of this paper is as follows:

1. Developing a six-element MIMO antenna with a novel decoupling structure for achieving better isolation. This design may be applicable to any planar MIMO antenna to realize a symmetrical structure with enhanced scalability.
2. Study of metallic surface effect on mmWave antenna performance such as on |S-parameter| and radiation pattern for V2V communication.
3. Estimation of channel capacity, path loss, and the link budget for 5G and V2V communication systems that employ the designed antenna for both LOS and NLOS conditions.

The flow of the article is as follows. Section II presents a six-element MIMO antenna and its DCS mechanism. Section III reports the results and discussion, followed by the antenna characterization for V2V communication in Section IV. Section V presents the comparative analysis, and Section VI concludes the article by summarizing its main remarks and providing future directions.

II. ANTENNA DESIGN METHODOLOGY

This section is devoted to present the structure of the six-element MIMO antenna as well as analyze the decoupling mechanism. The design and development of the single-element antenna of this MIMO structure is authors own contribution presented with detailed analysis in [15]. The reflection coefficient of a six-element MIMO antenna is analogous to the single-element antenna in [15], achieving

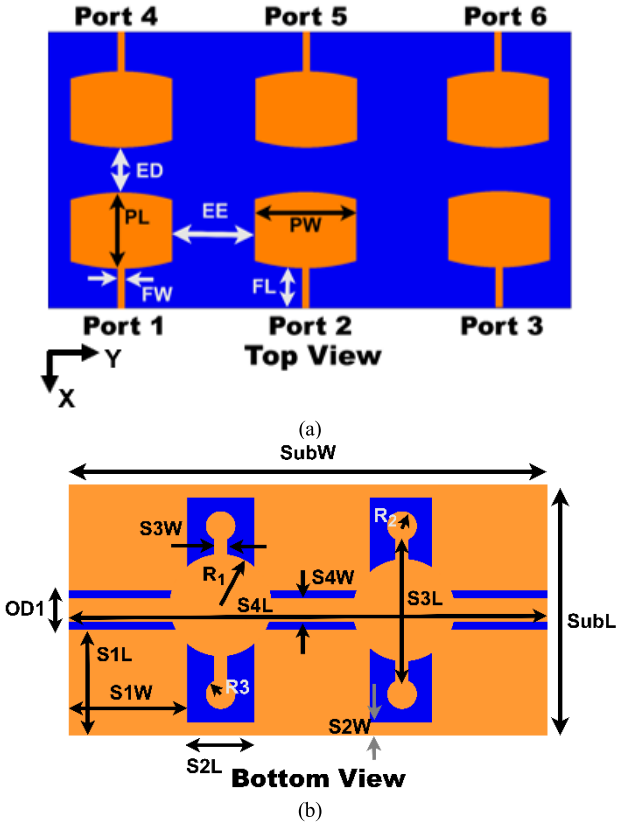

FIGURE 1. Proposed six-element MIMO antenna. (a) Top view, (b) Bottom view. The dimensions in mm are as follows: EE = 4, ED = 3.4, FL = 1.7, FW = 0.25, S1L = S1W = 6, OD1 = S2L = 3, S2W = S3W = 0.5, S3L = 9.58, S4L = 24, S4W = 1.6, R1 = 3, and R2 = R3 = 0.8.

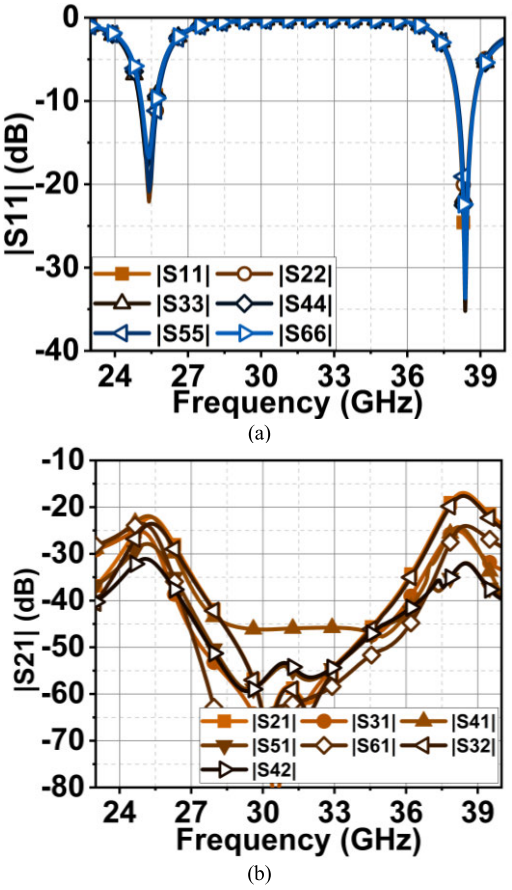

FIGURE 2. |S-parameter| response of proposed MIMO antenna. (a) Reflection coefficient |S11| graph. (b) Isolation |S21| graph.

dual-resonance at 25.5 GHz with TM_{10} mode and 38 GHz with TM_{02} modes.

A. SYMMETRICAL MIMO CONFIGURATION

The six-element MIMO antenna on Rogers 5880 substrate with its complex decoupling structure in the ground plane is illustrated in Figs. 1(a) and 1(b). The MIMO antenna has substrate length SubL = 15 mm and width SubW = 24 mm. The distance between the radiating elements is maintained close to half of the guided wavelength at 25.5 GHz, i.e., $\lambda_{0g} = c/f_0\sqrt{\varepsilon_r}$. It is to have the minimum effect from the near-field coupling. Thus, the three radiating elements of [15] are symmetrically arranged along the y-axis with an element-to-element (*EE*) distance of $0.5\lambda_{0g}$ in Fig. 1(a). The other three elements are vertically mirrored and separated by distance $ED = 0.43\lambda_{0g}$. This arrangement of radiating elements makes it a symmetrical configuration that can be scaled further to achieve higher-data-rate.

The ground plane has various shapes of structures of different lengths and widths, as displayed in Fig. 1(b). Each excitation port ground has a rectangular conductive surface (S1) of length S1L and width S1W. The port-grounds of 1, 2, 4, and 5 are connected by a circular stub of radius R1. Likewise, another R1 connects 2, 3, 5, and 6 port-grounds. This resolves the issues of disconnected ground as in [11], [13], and [14]. Further, the horizontal stubs (S2) are connected to the ports-ground with their length and width of S2L and S2W. The R1 is amended with a vertical stub that is terminated with R2 and R3. Also, a horizontal stub S4 is added, which connects the two circular stubs of R1. Therefore, the overall designed ground structure is complex, providing better isolation to adjacent, vertically opposite, and diagonally opposite elements.

The proposed MIMO antenna reflection coefficient (|S11|) and isolation (|S21|) graphs are shown in Figs. 2(a) and 2(b). The reflection coefficient response of all the six elements replicates each other exactly. It resulted in dual resonance at 25.4 GHz and 38.3 GHz. A slight drift in the resonances is observed due to modification in the ground plane. The simulated bandwidth at |S11| > 10 dB is 24.9-25.85 GHz and 38-38.9 GHz. The decoupling structure has provided better isolation |Sij| (where i ≠ j) of 22 dB except for |S52| at first resonance.

For |S52|, the isolation is at 16.5 dB. There are two reasons for this: i) the intermediate elements 2 and 5 are packed between other elements; ii) the first resonance gives rise to TM_{10} mode, which results in vertical polarization;

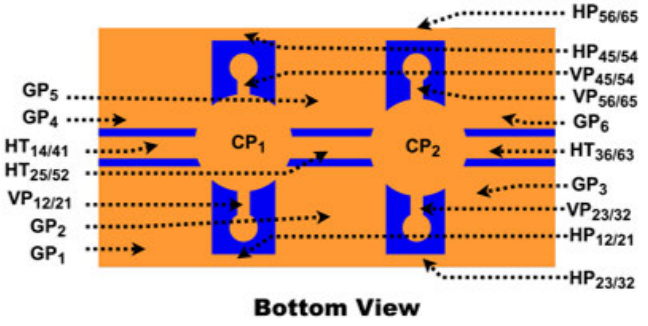

FIGURE 3. Proposed decoupling structure in the ground plane with structure terminologies.

consequently, the DCS structure guides partial surface wave current to the opposite intermediate element. Because of this, the isolation |S52|/|S25| is slightly hindered. However, the DCS structure neutralizes the surface wave of adjacent, diagonally opposite, and diagonally opposite elements. On the other hand, at the second resonance, |S52| is higher than 25 dB, whereas |S21| is at 17.5 dB due to TM_{02} mode. The surface wave coupling currents create signal correlation in MIMO antenna elements, thus lowering the antenna performance. However, an isolation level greater than 15 to 20 dB is desirable for efficient operation. Therefore, the coupling effects of our closely arranged MIMO antenna are within acceptable limits.

B. DECOUPLING MECHANISM

The proposed MIMO antenna adopts the decoupling structure technique in the ground plane to suppress the surface wave coupling. The proposed decoupling structure with its terminologies is displayed in Fig. 3. The terms GP_1 to GP_6 represent the port-grounds structure. The $HP_{ij/ji}$ and $VP_{ij/ji}$ (where i $\neq$ j) are the horizontal and vertical stubs that suppress the surface wave from the adjacent elements; that is, $HP_{12/21}$ and $VP_{12/21}$ provide the isolation between ports 1 and 2. Likewise, $HP_{23/32}$, and $VP_{23/32}$ provide isolation between ports 2 and 3, and so on. The $HT_{ij/ji}$ suppresses the coupling from opposite elements. The CP_1 and CP_2 regulate the coupling from diagonally opposite elements. The dimensions of the decoupling structure are tuned to balance the charge distribution satisfying the continuity equation (1) in the ground plane such that stringent electric fields are created using equation (2), suppressing the surface wave coupling.

$$\vec{\nabla}.\vec{J} + \frac{\partial \rho}{\partial t} = 0 \tag{1}$$

$$\vec{J} = \sigma \vec{E} \tag{2}$$

The oscillation of current from the excited antenna elements gives rise to surface waves in the substrate and ground plane through charge distribution. With the adequately tuned ground dimensions, the charges are distributed uniformly, neutralizing the coupling current. These coupling effects can be modeled with the Friss transmission equation (3) as defined in [16].

$$\frac{Prs}{Pts} = \frac{G_{st3}G_{sr3}\lambda_{0/1}^2}{(4\pi d_s)^2} + \frac{G_{st2}G_{sr2}\lambda_{0/1}}{4\pi d_s} + \frac{2G_{s3}G_{s2}\lambda_{0/1}}{4\pi d_s}\sqrt{\frac{\lambda_{0/1}}{4\pi^2 d_s}}\cos\left(\theta_{d_s}\right) \tag{3}$$

The first term in the above equation is the standard Friss equation with a 3D gain corresponding to the first or second resonance (25.5 or 38 GHz) of the excited and coupled antenna elements in the designed structure. The $d_s = EE\ or\ ED$ is the distance between excited and coupled antenna elements. The second term is surface wave coupling with 2D gain, and the third is the mutual phase difference effect with correcting factors G_{s3} and G_{s2}. The θ_{d_s} corresponds to the difference between the wavenumbers of surface-wave in the substrate (k_{sub}) and free-space (k_{fs}) multiplied by the distance d_s, as defined in (4).

$$\theta_{d_s} = \left(k_{sub} - k_{fs}\right).d_s \tag{4}$$

$$k_{sub} = \frac{2\pi f_{0/1}}{c\sqrt{\varepsilon_r \mu_r}} \tag{4a}$$

$$k_{fs} = \frac{2\pi f_{0/1}}{c} \tag{4b}$$

Here, the $f_{0/1}$ is the frequency at the first and second resonance, ε_r and μ_r are the relative permittivity and permeability of 2.2 and 1 for our Rogers 5880 substrate.

Furthermore, the working of the DCS mechanism can be better comprehended with the modal current vector representation in Figs. 4(b) and 4(d), which are extracted from the surface current vector at f_0 and f_1 in Figs. 4(a) and 4(c).

The general analysis of modal current is as follows: the current J_n^+ and J_n^- are the forward and reverse coupling currents from and to port-n when port-k is excited (where n & k = 1, 2, 3, 4). Let us assume that port-1 is excited. At f_0, in Fig. 4(b), the current J_1^+ and J_2^+ on stub $HP_{12/21}$, J_1^+ and J_2^+ on stub $VP_{12/21}$ has equal and opposite magnitude, canceling most of the current, resulting in isolation |S21| of 22.2 dB, as shown in Fig. 2(b). Likewise, the current J_1^- cancels J_3^- on stubs $HT_{14/41}$ and R1 resulting in |S41| of 22.2 dB. The coupling current J_1^+ decays with distance on a lossy conductive material at $\rho^{-1/2}$. Thus the J_1^+ has lower influence on ports 3, 5, and 6, resulting in the isolation of 27.5, 28.3, and 25 dB.

However, the situation is slightly different in the case of f_1. Here, the current oscillations are horizontal with TM_{02} mode; consequently, the J_1^+ has a strong influence on adjacent elements, which can be seen in Fig. 5(c). The J_1^+ magnitude is higher compared to J_2^+ on $HP_{12/21}$ resulting in isolation |S21| of 17 dB. However, J_1^+ effect is lower on port elements 3, 4, 5, and 6, resulting in isolation |S31|, |S41|, |S51| and |S61| of 25.5, 24.65, 32, and 24 dB, as displayed in Fig. 2(b). This similar analogy can be applied when other ports are excited.

These results are validated through (3) and (4) for port-1 excitation. Due to close-by elements, the transmitted

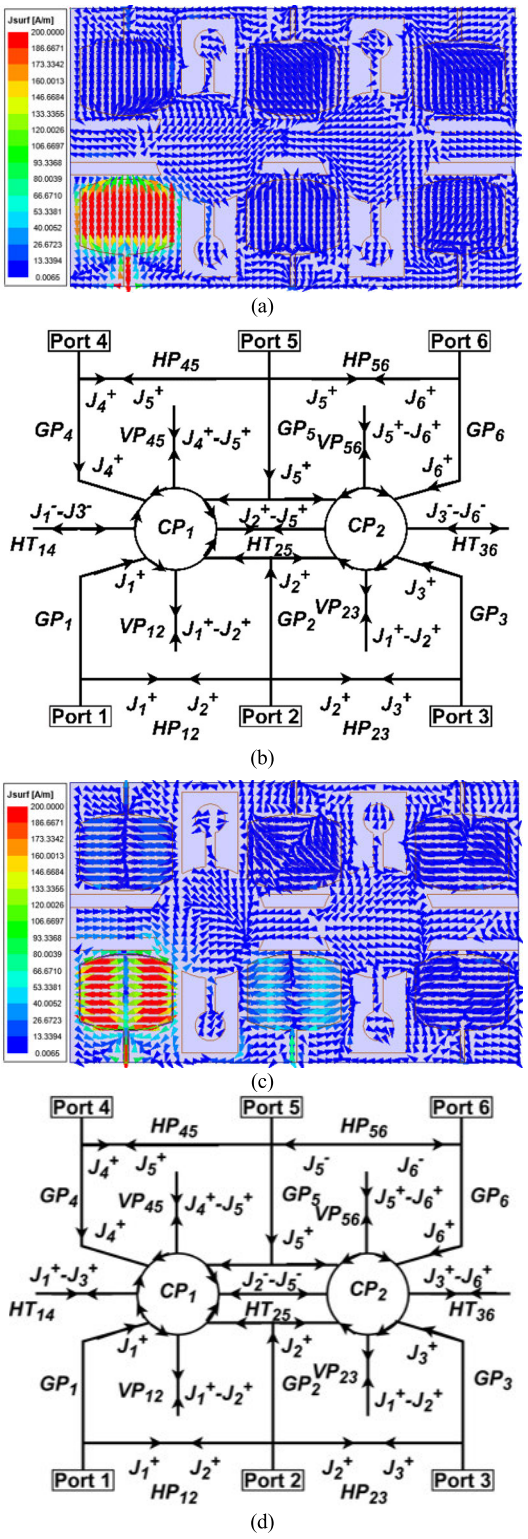

FIGURE 4. Surface vector current distribution at both the resonance frequencies with its derived modal vector current. (a) Surface vector current at f_0 with derived modal in (b). (c) Surface vector current at f_1 with its derived modal in (d).

and received gain is considered to be equal for our case. At first resonance (f_0), the 3D gain in the surface-wave direction is 1.4, and the 2D gain is 0.45. For the second

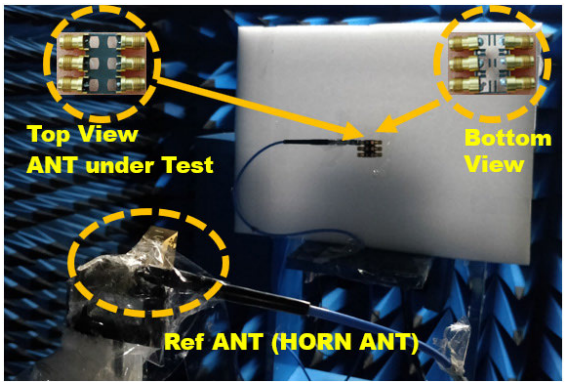

FIGURE 5. Anechoic chamber setup with prototype fabricated six-element MIMO antenna and reference Horn antenna for the radiation pattern measurement.

TABLE 1. $|S_{ij}|$ parameter comparison of simulated with theoretical analysis.

	Values at f_0		Values at f_1	
Parameter	Simulated	Theoretical	Simulated	Theoretical
|S21|	22.2	17.22	17	14.83
|S31|	27.5	49.84	25	32.24
|S41|	22.2	14.11	24.65	12.31
|S51|	28.3	25.53	32	21.19
|S61|	25	53.06	24	32.79

resonance (f_1), the 3D and 2D gains are slightly higher at 1.8 and 1.59 due to the TM_{02} mode. The value chosen for the correction factors $G_{s3} = G_{s2} = 0.1$. Considering the above values, the simulated and theoretical isolations are summarized in Table 1. The values in Table 1 indicate that the proposed decoupling structure has balanced the charged distribution, suppressing the surface wave coupling to the nearby elements. Therefore, with a little tuning, the proposed decoupling structure can be applied to any other MIMO antenna design, as in [9], [17], and [18], to achieve a symmetrical MIMO antenna configuration with enhanced isolation rather than non-scalable orthogonal configuration.

III. SIMULATED AND MEASUREMENT RESULTS OF MIMO ANTENNA

This section validates the designed antennas |S-parameter|, radiation pattern, and diversity parameters with prototype fabricated antenna measurements.

A. SCATTERING PARAMETERS AND RADIATION PATTERN

The designed antenna is a prototype, and its radiation pattern is measured in an anechoic chamber, as illustrated in Fig. 5. The |S-parameters| are measured using a KEYSIGHT N9951A vector network analyzer, which operates from 300 MHz to 44 GHz. The SMA connectors used are 2.4 mm from Johnson (147-0701-261), which operate up to 50 GHz. The simulated and measured first resonance occurs at 25.4 and 25.5 GHz, whereas the second resonance is observed at 38.3 GHz and 38 GHz,

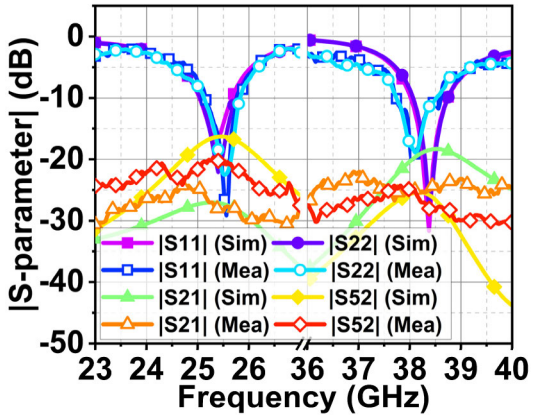

FIGURE 6. Simulated and measured |S-parameter| graphs of proposed antenna.

as displayed in Fig. 6. The achieved simulated and measured bandwidth at f_0 is 950 MHz, i.e., from 24.9 to 25.85 GHz, and 800 MHz, i.e., from 25.1 to 25.9 GHz. At f_1, it is 900 MHz, i.e., from 38 to 38.9 GHz, and 850 MHz, i.e., from 37.75 to 38.6 GHz. The simulated and measured percentage bandwidth at f_0 and f_1 are 3.72%, 2.34% and 3.13%, 2.23%, respectively. It is to be noted that, at mmWave, a small error in fabrication, port alignment, and soldering is expected to cause a vital deviation in simulation and experimental results. The second resonance and bandwidth deviation are due to fabrication and measurement tolerance.

However, the achieved results are within acceptable limits. The decoupling structure has resulted in a decent simulated and measured isolation |S21| of 28 dB and 26 dB at f_0 and 18 dB and 24 dB at f_1, respectively. The simulated and measured |S52| at f_0 are 16 dB and 20 dB, respectively. At f_1, it is 25 dB and 24 dB. Therefore, the overall measured isolation at both bands is higher than 20 dB.

The proposed antenna structure generates TM_{10} and TM_{02} modes at the first (f_0) and second resonance (f_1). As a result, at f_0, a beam is formed in the broadside direction with vertical polarization. Consequently, measurement is performed in XZ ($\phi = 0°$) and YZ-plane ($\phi = 90°$). The simulated and measured half-power beamwidth (HPBW) at f_0 is 72° and 63° (XZ-plane) and 70° and 68° (YZ-plane), respectively, in Figs. 7(a) and 7(b). The simulated and measured cross-polarization in the XZ-plane is -17.2 dB and in the YZ-plane is -21 dB. However, at f_1, TM_{02} mode forms two beams in the broadside direction with null at $\phi = 0°$ with horizontal polarization. Consequently, only YZ-plane measurement is performed. The simulated and measured HPBW are both equal to 68° in the YZ-plane with a dual beam at an angle of ± 30°, as depicted in Fig. 7(c). The simulated and measured cross-polarization is slightly higher in second band at -13.5 dB. The simulated peak realized gain of the proposed six-element MIMO antenna are 8.6 and 7.0 dBi at f_0 and f_1 bands. The measured gain is 9.0 and 7.2 dBi, respectively, as displayed in Fig. 7(d).

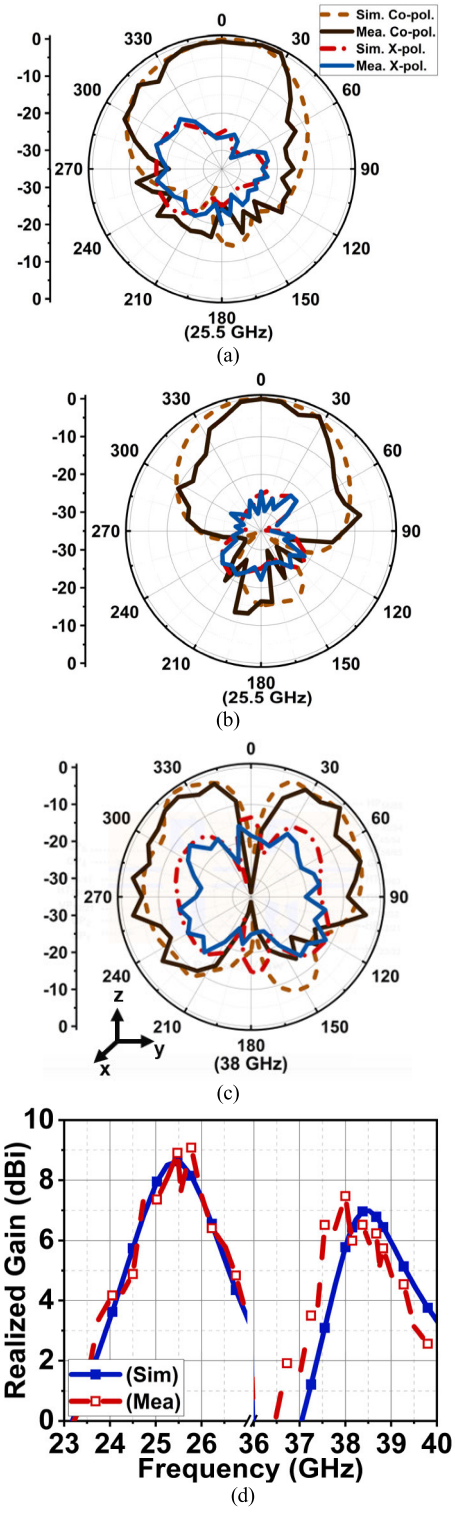

FIGURE 7. Normalized simulated and measured radiation patterns. (a) XZ-plane and (b) is YZ- plane at 25.5 GHz. (c) YZ-plane at 38 GHz. (d) Simulated and measured realized gain of proposed six-element MIMO antenna.

B. DIVERSITY PERFORMANCE

The designed MIMO antenna is validated for various diversity parameters, such as ECC, DG, CCL, and MEG.

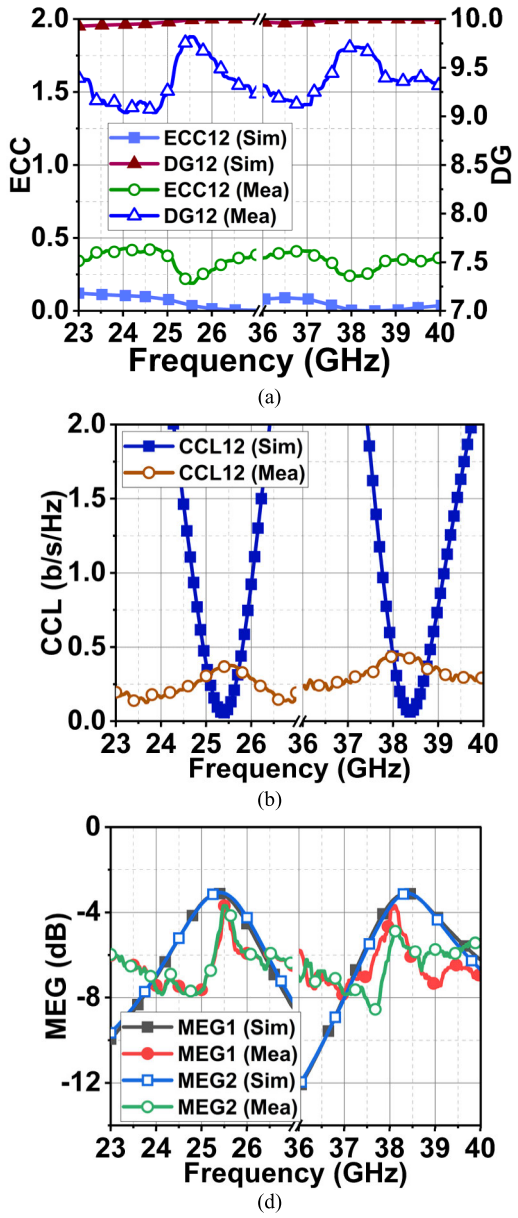

FIGURE 8. Diversity performance: (a) ECC and DG, (b) CCL, and (c) MEG.

The ECC defines the independent behavior of the radiation pattern of an individual element of MIMO antenna with low correlation to each other. In our case, the ECC is derived from the radiation pattern using the equation defined in [19]. Ideally, the ECC should be zero, but due to surface wave coupling, there will be some radiation correlation [20]. Acceptable ECC values should be no higher than 0.5. The results in Fig. 8(a) indicate the achieved simulated and measured ECC is less than 0.25 and 0.45 at both bands.

Therefore, the designed MIMO antenna radiation patterns can be considered uncorrelated. The DG defines the significant improvement in the MIMO element's signal-to-noise ratio (SNR) in contrast to a single element [21]. Ideally, DG should be 10. The measured DG is higher than 9.2 in all the observed frequency ranges, as shown in Fig. 8(a). The CCL defines the maximum throughput achieved by a MIMO antenna with a low bit-error rate (BER), which is calculated according to [22]. The universally acceptable CCL is less than 0.4 bits/sec/Hz. The simulated and measured CCL is less than 0.36 b/s/Hz for the MIMO antenna at both bands, as indicated in Fig. 8(b). The MEG is calculated using the methodology that was presented in [21]. The MEG should be less than −3 dB for an efficient MIMO antenna. The measured MEG is less than −3.5 dB, as displayed in Fig. 8(d). These results ensure that the proposed MIMO antenna provides acceptable diversity performance.

IV. V2V COMMUNICATION PERFORMANCE

The characterization of the proposed design is studied to corroborate its performance for V2V communication through channel capacity, path loss, and link margin at both the antenna resonances in LOS and NLOS conditions.

A. CHANNEL CAPACITY

The MIMO antenna enhances the channel capacity with a higher data rate and superior performance through spatial multiplexing and diversity performance. However, the actual throughput of the MIMO antenna depends on the channel conditions. The channel capacity of the MIMO antenna for an unknown channel state of information can be obtained as in [23] and [24].

$$C = B \log_2 \left[\det \left(\boldsymbol{I}_{N_r} + \frac{\rho_s}{N_t} \boldsymbol{H}\boldsymbol{H}^* \right) \right] \tag{5}$$

where B is the bandwidth, I_{N_r} is the identity matrix of the receiving antenna N_r, N_t is the number of transmitting antenna, ρ_s is the SNR, and $\boldsymbol{H}$ is the MIMO channel matrix.

For the measured bandwidth of 800 MHz and 850 MHz at 25.5 GHz and 38 GHz resonances, the channel capacity as a function of the SNR is shown in Figs. 9(a) and 9(b). At SNR of 30 dB, the six-element MIMO antenna supports up to 11 Gb/s and 9 Gb/s of data rate at 25.5 GHz and 38 GHz, respectively. On the other hand, the single-input-single-ouput (SISO) merely supports 3.5 Gb/s and 2.5 Gb/s data rates at 25.5 GHz and 38 GHz, respectively. However, if the MIMO antenna is exclusively used to enhance diversity, the data rate can be increased to more than 20 Gb/s.

B. EFFECT OF LARGE VEHICULAR METALLIC SURFACE ON ANTENNA PERFORMANCE

Prior to the analysis of V2V communication, the performance of the antenna over the vehicular body (large metallic surface) needs to be comprehended. The antenna is positioned on the vehicle at three points: A (rooftop), B (back side), and C (front side), as indicated in Fig. 10(a). The distance between the antenna and the vehicle surface is chosen to be 10 mm. Notice that this is the minimum required space to satisfy the boundary conditions during simulation. The computer-aided

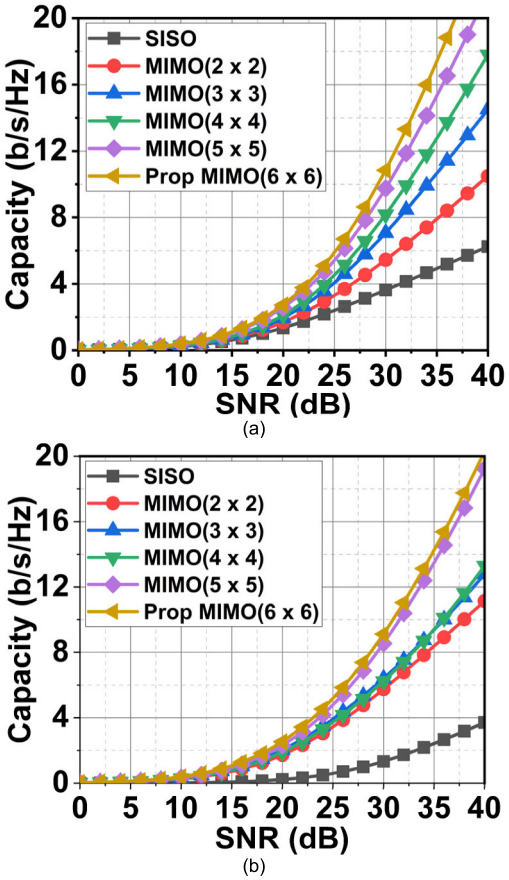

FIGURE 9. Channel capacity of the MIMO antenna vs SNR. (a) Capacity at first resonance. (b) Capacity at second resonance.

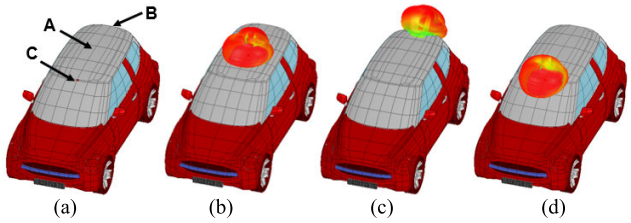

FIGURE 10. Effect of metallic structure on antenna radiation pattern at f_0. (a) Respective positions of antenna. Radiation pattern at (b) point A, (c) point B, and (d) point C.

TABLE 2. Antenna gain when placed at different locations of the vehicle.

Point	Frequency	Gain (dBi)
A (rooftop)	f_0	9.3
	f_1	10.1
B (back side)	f_0	8.2
	f_1	8.9
C (front side)	f_0	8.6
	f_1	8.7

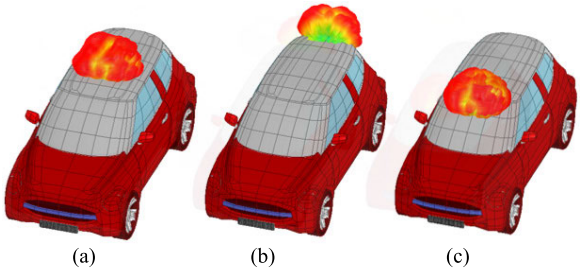

FIGURE 11. Effect of metallic structure on antenna radiation pattern at f_1. (a) At point A, (b) point B, and (c) point C.

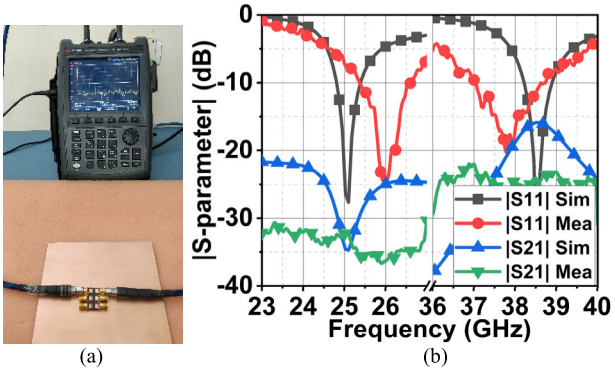

FIGURE 12. (a) |S-parameter| measurement setup on metallic sheet. (b) Corresponding simulated and measured results.

design (CAD) model considered in this case is a swift car with the material property of a perfect electric conductor (PEC).

The electromagnetic wave interaction of an antenna with a large metallic surface (car body) is analyzed through high-frequency simulation software (HFSS) using a shooting and bouncing ray (SBR) tool. The mmWave antenna is considerably smaller compared to large vehicle dimensions. Hence, the SBR+ performs complex meshing of large objects and computes the antenna behavior over a large metal structure as infinite ground. In this case, a negative image current forms on the metallic surface, spreading radiated energy over the azimuthal plane, which distorts the pattern, as shown in Figs. 10(b-d) at f_0 and Figs. 11(a-c) at f_1. However, it increases the front-to-back ratio [25] from 20.6 dB to 33.89 dB, resulting in increased gain, as presented in Table 2. The measurement setup of the |S-parameter| of the proposed antenna with the metallic surface is shown in Fig. 12(a). The measured results in Fig. 12(b) show a slight deviation in the first resonance due to the metallic surface effect.

Fig. 13 shows the corresponding simulated and measured radiation patterns. The radiation pattern is measured by placing a large metallic sheet below the antenna in an anechoic chamber. Due to the effect of the metallic sheet, the radiation pattern is slightly distorted, however, the front-to-back ratio is increased, as a result the simulated and measured HPBW at f_0 is 48° and 36° in XZ-plane; 70° and 63° in YZ-plane, respectively. Likewise, at f_1, the simulated and

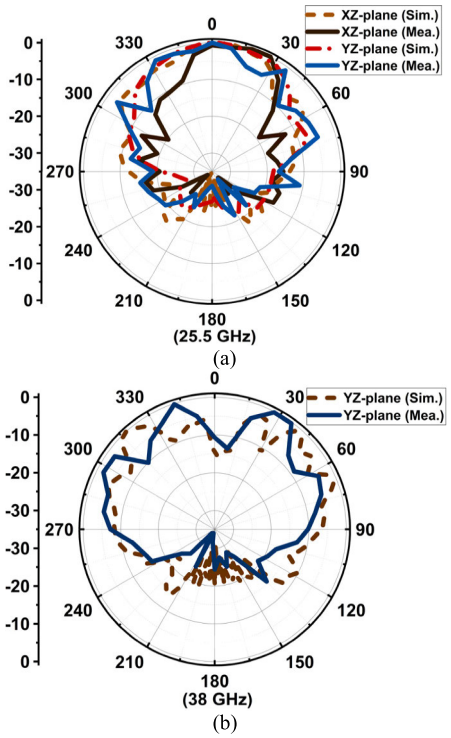

FIGURE 13. Normalized simulated and measured pattern over a metallic sheet. (a) XZ and YZ plane at f_0. (b) YZ plane at f_1.

measured HPBW in YZ-plane is 18° and 27° (with two beams tilted at ±30°).

C. PATH LOSS ANALYSIS FOR V2V COMMUNICATION

For V2X communication, as per the third generation partnership (3GPP) release 14, the effective freeway communication distance is 320 m with a maximum latency of 100 ms [26]. Therefore, we considered the V2V communication at 5G scenario to study the path-loss and link margin of the proposed antenna up to 40 m distance.

The outdoor propagation model with LOS and non-LOS (NLOS) scenarios with four test cases for each resonance [27] (f_0 and f_1) are considered, as illustrated in Figs. 14(a) and 14(b). For all the scenarios, the TX vehicle is assumed to be moving at a constant Z km/h speed along the x-direction and the RX vehicle in the same direction with 2Z km/h speed. The following are the test case scenarios:

- Case I: The transmitting antenna (TX) and receiving antenna (RX) are positioned at point A on two vehicles. Both antennas have clear LOS conditions without obstruction.
- Case II: The TX is positioned at point B (back side) on vehicle 1, and the RX antenna at point C (front side) on vehicle 2. Both antennas are directionally aligned and have direct LOS conditions.
- Case III: The TX and RX antennas are positioned similarly to case I, but a truck between the two vehicles creates obstruction, resulting in NLOS condition.

TABLE 3. Parameters considered in the analysis of path loss models.

Environment		LOS		NLOS	
Parameters		f_0	f_1	f_0	f_1
$P_{tf_x}(dBm)$		29.86	29.83	29.86	29.83
G_{tpf_x}(dBi) & G_{rpf_x}(dBi)	A	9.3	10.1	9.3	10.1
	B	8.2	8.9	8.2	8.9
	C	8.3	8.7	8.6	8.7
TX height (m)		1.5			
RX height (m)		1.5			
PLE n		2.5		5.4	
σ		3.5		14.8	
α_{LOS}		1.25		0.319	
α_{FI}		3.9		2.5	
β_{FI}		31.8		80.6	
α_{ABG}		1		2.8	
β_{ABG}		55		46.7	
γ_{ABG}		1.7		1.9	
σ_{ABG}		2.9		4.3	

- Case IV: The TX and RX antennas are positioned similarly to case II. A truck creates NLOS condition.

The outdoor propagation model (highway terrain) for V2V communication is simulated using the HFSS Savant tool. Under the LOS condition, the received signal is the sum of the direct LOS and ground-reflected signals. On the other side, the low mount of the antenna on the vehicle or obstruction caused by the other vehicles may lead to NLOS conditions [3]. In such cases, multipath signals aid in signal reception. The performance efficiency of the proposed antenna for the LOS and NLOS conditions is computed through path loss analysis.

The transmitted power, gain of transmitting and receiving antenna, and received signal are required to calculate the path loss. The tool estimates the received signal based on the simulation setup. We have set the number of shooting rays to 3 and bounces to 2 in the tool to reduce the computation time. Thus, a trade-off is made between accurate modeling and computation time. The path loss from the estimated received signal can be calculated as

$$PL = P_{tf_x}(dB) - P_r(dB) + G_{tpf_x} + G_{rpf_x} \quad (6)$$

where P_{tf_x} is the transmitted power in dB at f_0 and f_1, P_r is the received power (obtained from the tool), which includes multipath effect and losses, G_{tpf_x} and G_{rpf_x} is the gain of TX and RX for different antenna positions and resonance frequencies, as mentioned in Table 2.

The computed path loss is compared with the existing seven large-scale path loss models, such as Friis free-space path loss (FS), Stanford University Interim (SUI), Close-In (CI), modified FS, modified SUI, floating-intercept FI, and alpha-beta-gamma model (ABG). These path loss models are constructed using the methodologies that were presented in [28], [29], and [30]. Table 3 provides the values considered for analyzing and constructing these path loss models.

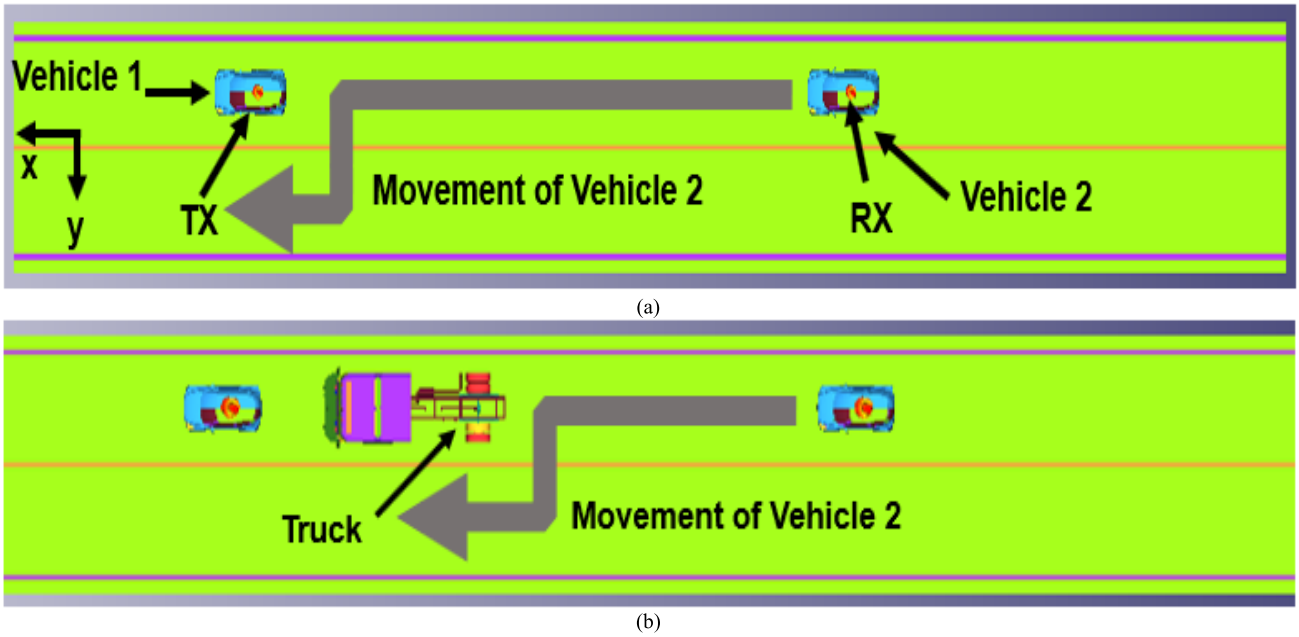

FIGURE 14. Outdoor V2V propagation secnario. (a) LOS and (b) NLOS scenarios.

The FD equation can be calculated as

$$PL_{FS}(d) = -10.\log_{10}\left(\frac{G_{tpf_x}G_{rpf_x}\lambda^2}{(4\pi d)^2}\right) \tag{7}$$

where λ is the carrier wavelength and d is the distance in meters. Of note (7) only considers the frequency and distance effect. However, the path loss will be much higher in real-time due to other losses and shadow effects, which FS does not include.

The SUI model is well-suited for path loss calculations for the carrier frequencies above 2 GHz. It returns the path-loss value as

$$PL_{SUI}(d) = PL(1m) + 10n\log_{10}\left(\frac{d}{1m}\right) + X_{f_c} + X_{RX} + X_\sigma \tag{8}$$

where

$$PL(1m) = 20.\log_{10}\left(\frac{4\pi(1m)}{\lambda}\right) \tag{8a}$$

$$n = a - b.h_{TX}(m) + \frac{c}{h_{TX}(m)} \tag{8b}$$

$$X_{f_c} = 6.\log_{10}\left(\frac{f_{MHz}}{2000}\right), \quad f_c > 2\text{GHz} \tag{8c}$$

$$X_{RX} = -20.\log_{10}\left(\frac{h_{RX}}{2}\right) \tag{8d}$$

Since the virtual environment setup under investigation is flat and rare vegetation, SUI Terrain type C parameters ($a = 3.6$, $b = 0.005$, and $c = 20$) are chosen to calculate the path loss exponent (PLE), n. The X_{f_c} and X_{RX} are the additional correcting factors that is carrier frequency and receiver height in the SUI model. Notice that (8) also considers the shadowing effect, X_σ, which has a 0 dB mean and standard deviation σ range between 8.2 dB and 10.6 dB.

The CI model is a variant of SUI that neglects the frequency and receiver height correction factors. It can be obtained as

$$PL_{CI}(d) = PL(1m) + 10n\log_{10}\left(\frac{d}{1m}\right) + X_\sigma \tag{9}$$

The FS model is further tuned to incorporate the additional losses by adding the slope correction factor α_{LOS}, which provides closer results to CI LOS model. It is obtained as

$$PL_{FS,Mod}(d) = \alpha_{LOS} \times (PL_{FS}(d) - PL_{FS}(1m)) + PL(1m) + X_\sigma \tag{10}$$

In the case of the NLOS environment, the SUI model is modified to closely fit in with the CI NLOS model with a slope correction factor , α_{NLOS}. This model is described by

$$PL_{SUI,Mod}(d) = \alpha_{NLOS} \times (PL_{SUI}(d) - PL_{SUI}(1m)) + PL(1m) + X_\sigma \tag{11}$$

The CI model in (9) works for the single-frequency data set, as it has only PLE that must be tuned to obtain the desired result. Similarly, the floating-intercept (FI) model works on the single-frequency data set. It is calculated by considering the coefficient α that dependents on the transmission distance, floating intercept in dB, and shadow effect (X_σ). The model can be described by

$$PL_{FI}(d) = 10\alpha_{FI}\log_{10}(d) + \beta_{FI} + X_\sigma \tag{12}$$

The multi-frequency path loss model uses the alpha-beta-gama (ABG) model. It has three variables to tune α_{ABG},

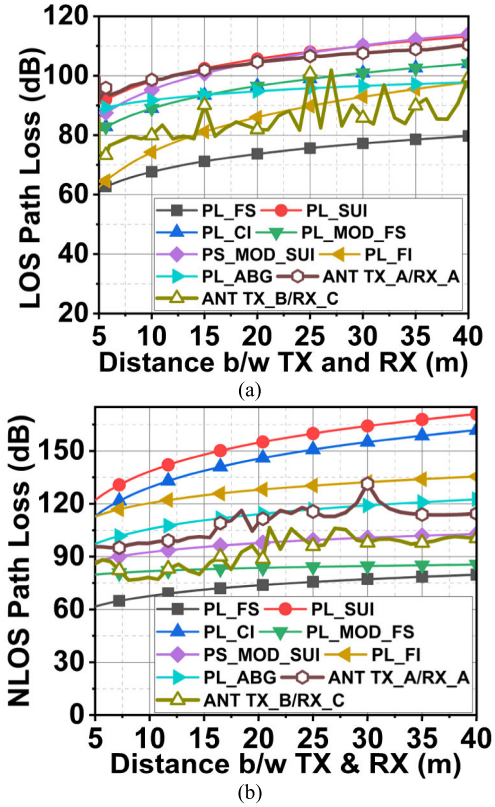

FIGURE 15. Computed path loss of proposed antenna under LOS and NLOS environment at f_0 and compared with existing models. (a) For cases I and II. (b) For cases III and IV.

β_{ABG}, and γ_{ABG}. The α_{ABG} and γ_{ABG} represent the path loss dependence on distance and frequency. The β_{ABG} represents optimized offset (floating) path loss. It is calculated as:

$$PL_{ABG}(d) = 10\alpha_{ABG}\log_{10}\left(\frac{d}{1m}\right) + \beta_{ABG} + 10\gamma_{ABG}\log_{10}\left(\frac{f}{1GHz}\right) + X_{\sigma_{ABG}} \quad (13)$$

1) CASE – I AND CASE -II AT f_0

The simulated path loss for case I at f_0 is where the TX and RX antennas are positioned at point A. In this case, the radiated energy is spread in the azimuthal plane due to the antenna placed at the center of a large metallic sheet. Consequently, the received signal is mostly free from the reflected signals, and the received signal is mainly direct LOS. The results in Fig. 15(a) show a gradual increase in path loss from 93 to 110.3 dB with increasing distance between TX and RX from 5 to 40 m. Compared with other models, the estimated case I closely follows the SUI and modified SUI path loss model. The CI and modified Friss can be also considered accurate.

In the case II, the TX antenna is placed at point B and RX at point C. In this case, the path loss is reduced due to directional antenna alignment. The estimated path loss ranges from 73.27 to 99.42 dB, as displayed in Fig. 15(a). However, a sudden surge in path loss at a certain distance is due to the multipath signals. These TX and RX antenna position points are prone to multipath effects [31], which sometimes have destructive effects. The obtained results closely align with the FI and Friss path loss models.

2) CASE – III AND CASE -IV AT f_0

In an NLOS scenario, a truck is introduced as an obstruction between the transmitting and receiving vehicles. In Case III, both antennas are placed at point A. Compared to case I, the path loss attenuation is marginal, with a lower and higher path loss limit of 95 and 114.4 dB. However, in NLOS, the multipath signals contribute to the received signal. In this case, the sudden path loss surges are due to the shadowing effect and diffraction of signal from the sharp edges of the truck and road [31]. It can be seen in Fig. 15(b) at 17 and 30 m. The computed path loss fit in with the ABG model.

In case IV, the TX antenna is placed at point B and the RX antenna at point C, which increases the SNR due to the LOS alignment of TX and RX. It improved the path loss to 100.8 dB at a 40 m and with a lower limit of 76.6 dB at a 5 m distance, as displayed in Fig. 15(b). The computed path loss closely follows the modified SUI and partially with the modified Friss model.

3) CASE – I AND CASE – II AT f_1

As discussed in Section III, the proposed antenna generates TM_{02} mode at f_1. In this case, antennas are made to communicate with vertical polarization by mechanically rotating the antenna over the vehicles. For case I, the estimated lower and upper path loss limits are 91.7 dB and 108.46 dB at f_1, as shown in Fig. 16(a). However, for case II, the path loss is higher, between 103.27 dB and 116.94 dB, as shown in Fig. 16(a). The antennas at points B and C have acceptable directional alignment. However, due to TM_{02} mode, these positions have higher multipath effects, resulting in increased path loss compared to case II at f_0. The computed path loss for the case I condition at f_1 fits the CI and modified Friss path loss model. Case II lies between the SUI and CI models.

4) CASE – III AND CASE – IV AT f_1

Under NLOS conditions, the estimated path loss has achieved almost similar results for cases III and IV at f_1. For case III, the path loss range is 105.7 dB and 116.9 dB, as presented in Fig. 16(b). For case IV, it is 90.76 dB and 126.85 dB, in Fig. 16(b). In case IV, the sudden surges in the path are due to shadowing and blockage effects.

Therefore, from the above analysis, it can be concluded that the proposed antenna provides smooth path loss fading for case I at f_0 with slightly higher limits than case II. Case II has resulted in lower attenuation of signals. However, due to antenna positions, a sharp increase in path loss at certain

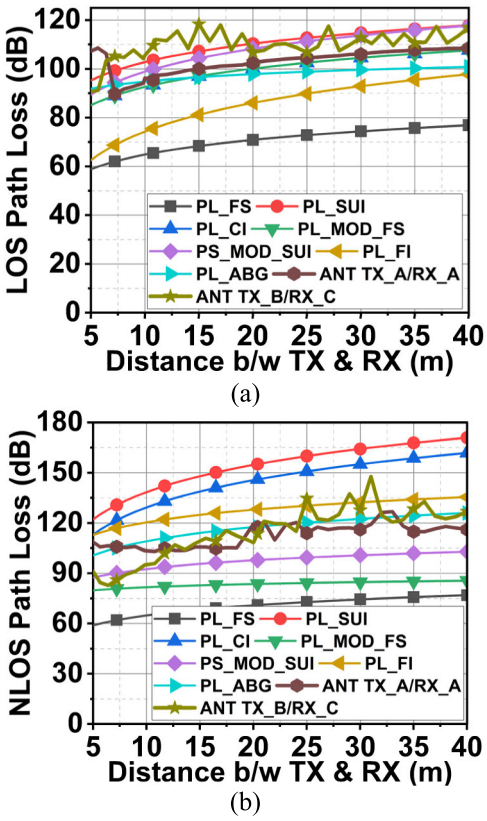

FIGURE 16. Computed path loss of proposed antenna under LOS and NLOS environment at f_1 and compared with existing models. (a) For cases I and II. (b) For cases III and IV.

distances can be seen. Under NLOS conditions, these test cases have performed well at f_0. At f_1, the path loss is better in case I compared to that of f_0. However, for case II (at f_1), the path loss is higher and appears to be independent of distance. A similar response can be seen for case III, whereas in case IV, path loss increases with sharp spikes.

D. V2V COMMUNICATION LINK MARGIN

The link budget estimation provides information about the effective communication distance over the channel, considering transmitted power, antenna gain, noise, and other losses [32]. Considering the computed received power (P_r) from the section IV-C link margin (LM) in dB is calculated for cases I to IV V2V communication. It can be obtained as

$$LM = P_r - R_p \tag{14}$$

where the R_p is the required power to establish reliable communication in a lossy environment and is given in dBm. Considering a binary phase shift keying (BPSK) modulation with a BER of 10^{-6}, the required energy per bit, E_b, to noise, N_0 ratio (E_b/N_0) is 9.6 dB [33]. Therefore, the required power R_p can be calculated as

$$R_p = \frac{E_b}{N_0} + KT + 10\log_{10}(B_r) \tag{15}$$

where K is the Boltzmann constant (1.38×10^{-23}J/K), T is the temperature in kelvin (K), which is set to 290 K. N_0 stands for the noise power density, which is set to -199.9 dB/Hz. The B_r is the various bit rates considered in our analysis ranging from 1 Mb/s to 10 Gb/s.

The antenna link margin for cases I to IV for both frequencies f_0 and f_1 is computed and presented in Figs. 17 and 18. Next, by assuming a link margin of 0 dB aids in reliable V2V communication, we observe the link budget for all the above cases. At f_0 for case I, the proposed antenna can support 10 Gb/s of data rate up to 15 m. However, 1 Gb/s of data is supported up to 40 m, as presented in Fig. 17(a). For case II at f_0, 10 Gb/s of data is supported for more than 40 m, as displayed in Fig. 17(b). For NLOS condition in case III at f_0, the proposed antenna can support 500 Mb/s of data to 40 m, as illustrated in Fig. 17(c). However, in case IV at f_0, data rate support is higher than 10 Gb/s for more than 40 m, as depicted in Fig. 17(d).

At the second resonance (f_1) for case I, the antenna supports 10 Gb/s of data rate up to 40 m, as shown in Fig. 18(a). However, the maximum supported data rate for case II is 1 Gb/s, as in Fig. 18(b). For cases III and IV in Figs. 18(c) and 18(d) is 10 Gb/s up to 15-20 m. However, 200-500 Mb/s of data is easily supported up to 40 m distance in all these cases. From the above analysis, it can be concluded that the performance of the proposed antenna is dependent on the antenna position on the vehicle and LOS and NLOS conditions.

E. ANTENNA MOUNTING AND V2V ARCHITECTURE

The above analysis indicates that the reflections (from ground and objects) and path loss are severe at mmWave frequency. The V2V communication at mmWave demands a directional antenna to compensate for higher path loss attenuation. Thus, the proposed MIMO antenna possesses a directional radiation pattern with good gain. The performance is further improved by narrowing the beam by adopting a beamforming network (BFN) for the proposed MIMO antenna. In our case, three of the six radiating elements can be used for beamforming during transmission, and the rest can be used for reception. With the phased array technique, a small form factor BFN can be achieved [34]. With BFN, the antenna could also perform beam scanning. However, with highly directional radiation, an issue of overhearing occurs [35], which can resolved by mounting four proposed MIMO antenna at points A, B, and C, as shown in Fig. 19.

As mentioned before, due to high reflections, the mmWave frequency cannot easily penetrate inside the vehicle due to the metallic body. Therefore, the antennas can be mounted on the rooftop for better V2V communication. The antenna is covered with a radome to protect it from harsh environmental conditions. A multilayer radome such as A-sandwich or B-sandwich is appropriate for the proposed MIMO antenna with BFN employed. It ensures wide bandwidth and good

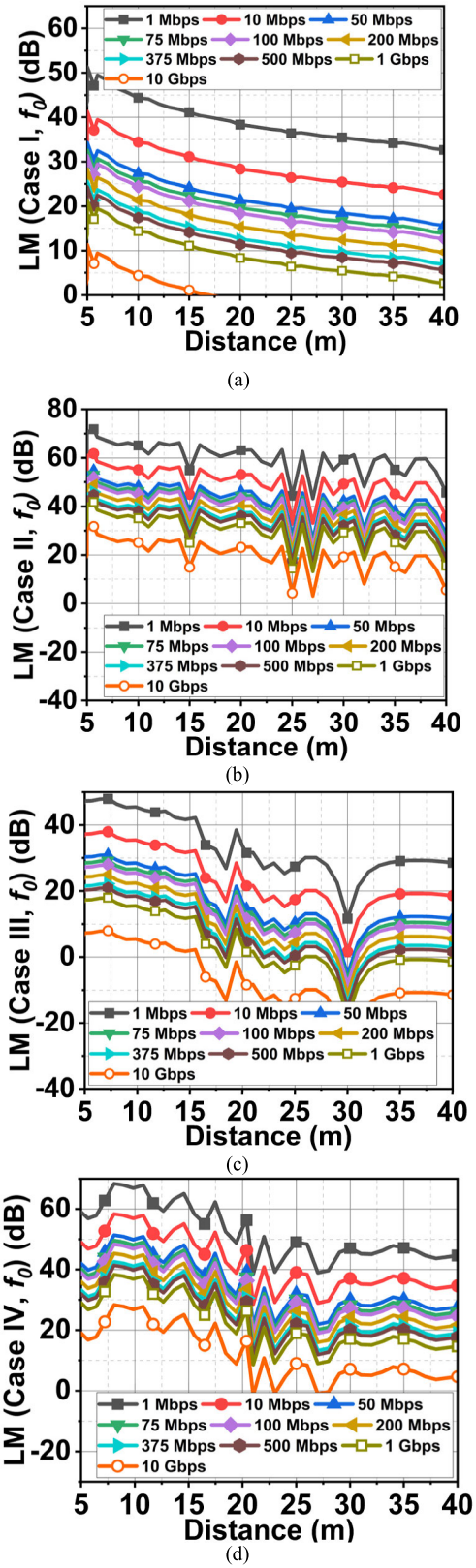

FIGURE 17. Link margin estimation for the proposed antenna at f_0. (a) LM for case I, (b) LM for case II, (c) LM for case III, (d) LM for case IV.

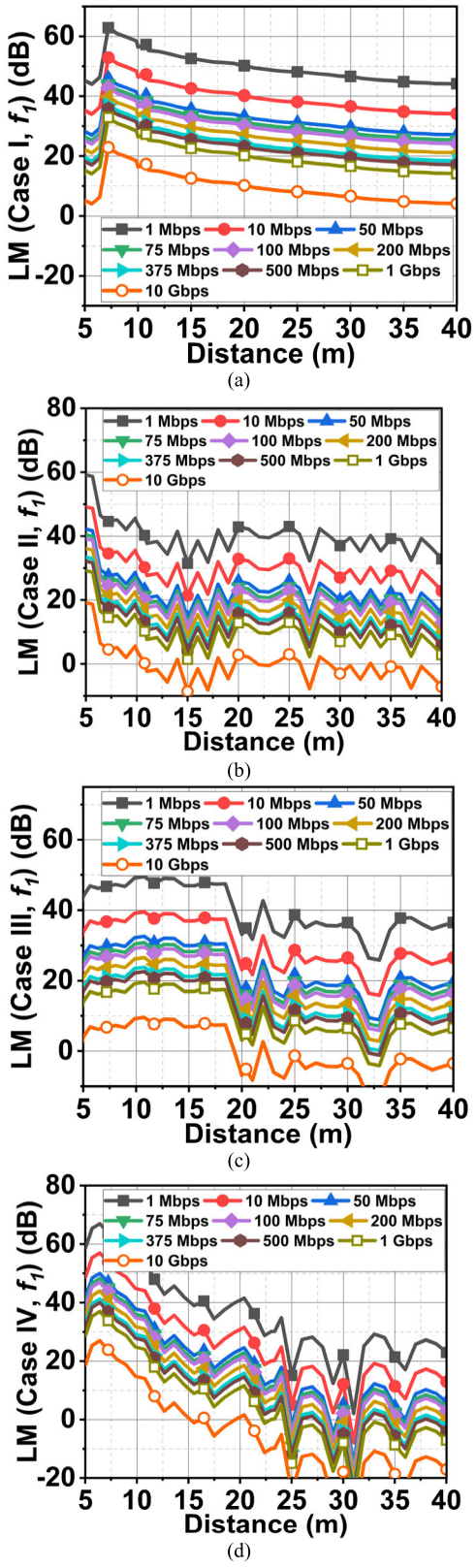

FIGURE 18. Link margin estimation for the proposed antenna at f_1. (a) LM for case I, (b) LM for case II, (c) LM for case III, (d) LM for case IV.

scanning angle with minimum RF reflections [36]. Such double-layer radomes can be made from metamaterial structures on thin substrate [37], inverse-pyramid corrugation structure [38], and so on.

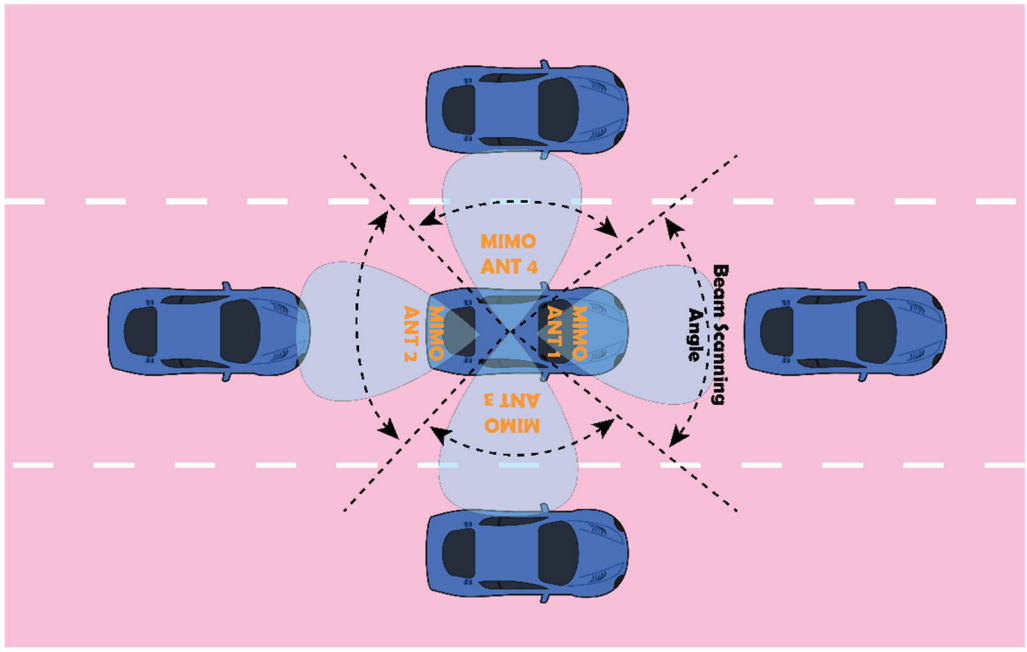

FIGURE 19. Four sets of MIMO antenna mounting at points A, B, and C with BFN for beam scanning to achieve better V2V Communication.

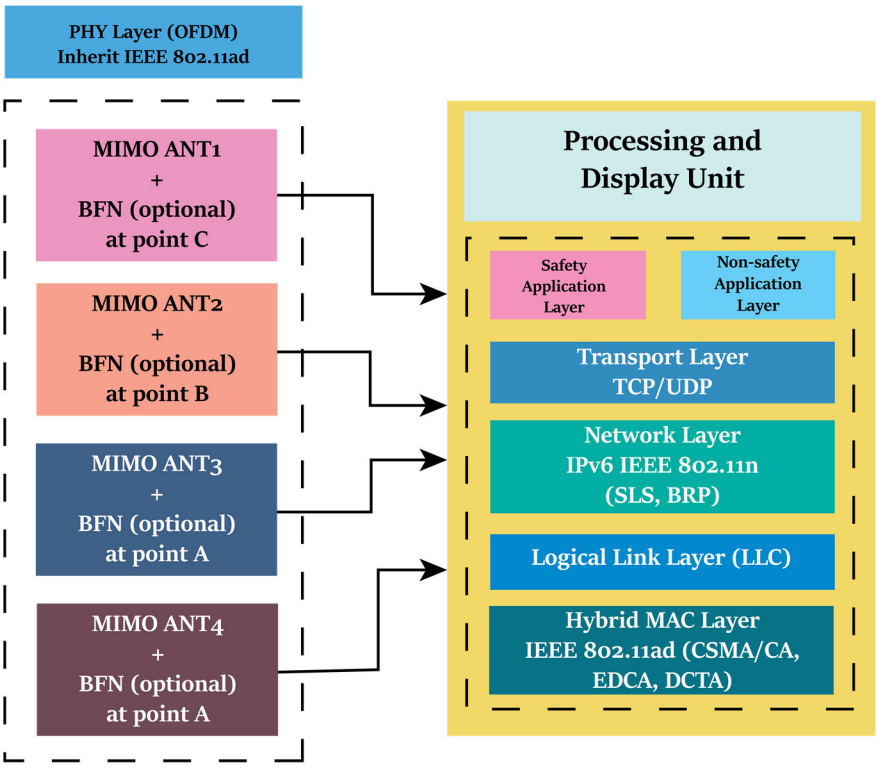

FIGURE 20. V2V mmWave device architecture presenting proposed antenna in the physical layer to its interface till application layer.

As per 3GPP Release 14, the V2V architecture must have connectivity with the vehicles moving at an absolute speed of 140 km/h and 60 km/h in freeway and urban areas. Now, it is the responsibility of the MAC layer to ensure connectivity. Any misalignment of directional antennas or scanning mismatch leads to a deafness

TABLE 4. Comparative analysis of proposed MIMO antenna with existing state-of-art designs.

Ref.	Ant Type	STR	Dim-ension @ λ_0	No. of Port	Res. (f_0)	BW |S11| (GHz)	Iso. |S21| (dB)	Max Gain (dBi)	D-Scl.	GD	ECC	DG	CCL (b/s/ Hz)	MEG (dB)	PL & LM
[7]	PRP+ SL	Sym.	$1.2\lambda_0 \times 3.01\lambda_0$	4	30	29-37.5	> 16	9.5	YES	NA	< 0.01	> 9.7	NA	NA	NO
[14]	PRP	3D	$4.95\lambda_0 \times 4.95\lambda_0$	12	28	22.5-29.8	NA	6	NO	Dis	NA	NA	NA	NA	NO
[42]	PRP	Orth.	$3.09\lambda_0 \times 3.09\lambda_0$	4	28	25-50	> 18	NA	NO	Dis	< 0.005	> 9.99	< 0.25	NA	NO
[43]	PRP	Sym.	$1.12\lambda_0 \times 4.49\lambda_0$	4	28/ 40	24-33/ 37-41	> 21	4.9	YES	Dis	< 0.000 5	> 9.99	NA	NA	NO
[44]	PRP+ SL	Orth.	$4.07\lambda_0 \times 4.07\lambda_0$	4	28/ 38	27.5-28.6/ 37.2-38.7	> 25	7.9 / 13	NO	Con	$< 2.5 \times 10^{-4}$	> 9.99	< 1	< 3	NO
[45]	PRP+ SL	Orth.	$4.16\lambda_0 \times 4.16\lambda_0$	8	24	23.5-27.6	> 26	8	NO	Con	< 0.000 4	> 9.99	NA	NA	NO
[46]	PRP+ SL	Sym.	$2.34\lambda_0 \times 2.46\lambda_0$	4	28	27.5-60	> 25	10	YES	Con	< 0.007	> 9.965	NA	NA	NO
[47]	ML+ SCL	Arb.	$1.5\lambda_0 \times 1.5\lambda_0$	3	24	23.5-24.5	> 22	4.5	YES	Con	NA	NA	NA	NA	NO
Proposed	**PRP**	**Sym.**	**$1.28\lambda_0 \times 2.04\lambda_0$**	**6**	**25.5/ 38**	**25.1-25.9/ 37.75-38.6**	**> 20**	**9 / 7.2**	**YES**	**Con**	**< 0.25**	**> 9.999**	**< 0.36**	**< 3**	**YES**

Note: Ant – antenna, STR – structure, BW – bandwidth, Iso. – isolation, D-Scl. – design scalability, GD – ground connection, PL and LM – pathloss and link margin estimation, NA – Not available, Con – Connected ground plane, Dis- Disconnected ground plane. PRP – Planar patch, SL- Sloted, ML- Multilayer, SCL- Slot coupled, Sym. – symmetrical, Orth. – orthogonal, Arb. – arbitrary.

effect. Also, the long congestions lower the V2V throughput.

The proposed MIMO antenna and the existing antennas in the literature operating in a similar band [34], [39], [40] may adopt the IEEE 802.11ad mmWave standard for better V2V communication. The Ka-band frequencies have wave characteristics similar to 60 GHz with less attenuation. Thus, the IEEE 802.11ad standard for 60 GHz may also be suitable for Ka-bands. The V2V communication device has an antenna unit on the vehicle connected to the processing unit through RF cables. The processing unit is also embedded with the display unit, as shown in Fig. 20.

The physical layer in IEEE 802.11ad adopts the orthogonal-frequency-division-multiplexing (OFDM) to achieve higher data. Before that, it uses a 32-bit Golay spreading sequence with binary-phase-shift-keying (BPSK) modulation to establish the communication between the vehicles [35]. To achieve communication with higher data of 6.75 Gb/s, 64-QAM is implemented. The mmWave architecture follows enhanced distributed channel Access (EDCA) and dynamic channel time allocation (DCTA) to handle traffic congestion, frame aggregation, and channel access polling. The logical link layer (LLC) handles the flow and error controls [41].

The IEEE 802.11ad architecture adopts a beam training technique, which was missing in IEEE 802.11p. It initiates the beam training process through the frame sequence in two phases. During the first sector-level sweep (SLS) phase, the antenna sector is configured. Later, the beam refinement phase takes place through the beam-refinement protocol (BRP). Above these are the transport layer and application layer. The application layer has two subsections to handle the safety and non-safety information. Thus, the V2V device architecture at mmWave is sophisticated enough to deliver higher data with other vehicles while handling better connectivity and congestion.

V. COMPARATIVE ANALYSIS

The performance of the proposed antenna is compared with the existing state-of-the-art designs, as summarized in Table 4. The antenna element structure is simple yet generates dual resonance compared to other existing designs. The antenna is compact compared to [14], [42], [43], [44], [45], and [46]. The proposed antenna has resulted in a descent

bandwidth comparable with [44] and [47]. The antenna has acceptable isolation compared to [42], [43], and [47]. The antenna also resulted in an acceptable gain compared to [14], [43], [45], and [47]. Moreover, the design is scalable to n-element MIMO antenna, which few of the designs support. The proposed MIMO antenna is validated for all the diversity parameters. The article also calculated the path loss and link margin of the proposed antenna for V2V communication in highway scenarios, which other designs neglect.

VI. CONCLUSION

This article presents a dual-band six-element MIMO antenna with a compact structure for V2V communication. The antenna generates the first resonance at 25.5 GHz with TM_{10} mode and the second at 38 GHz with TM_{02} mode operating at n258 and n260 band. The proposed novel DCS provides isolation that is more than 20 dB at 25.5 GHz and 38 GHz. The measured bandwidth range of the proposed antenna at both the resonances is 25.1-25.9 GHz and 37.75-38.6 GHz. The antenna radiates energy in the broadside direction with good gain. The antenna is validated for ECC, DG, CCL, and MEG diversity parameters. It supports a channel capacity of 6 Gb/s for an SNR of 30 dB; however, it is dependent on the distance. The estimated path loss under LOS and NLOS conditions ranges from 73.27 to 126.85 dB for a 5-40 m distance. As per LM calculation, the proposed antenna supports 10 Gb/s of data under particular LOS and NLOS conditions. However, the 500 Mb/s data rate is supported for any LOS and NLOS conditions. These features ensure that the six-element MIMO antenna is a competitive candidate for V2V communications operating at the mmWave band. This work could be further expanded to an array-based MIMO antenna to achieve improved bandwidth and narrow beam radiation pattern for better performance of V2V communication scenarios.

REFERENCES

[1] S. Zeadally, M. A. Javed, and E. B. Hamida, "Vehicular communications for ITS: Standardization and challenges," *IEEE Commun. Standards Mag.*, vol. 4, no. 1, pp. 11–17, Mar. 2020, doi: 10.1109/MCOMSTD.001.1900044.

[2] N. K. Mallat, M. Ishtiaq, A. Ur Rehman, and A. Iqbal, "Millimeter-wave in the face of 5G communication potential applications," *IETE J. Res.*, vol. 68, no. 4, pp. 2522–2530, Jul. 2022, doi: 10.1080/03772063.2020.1714489.

[3] R. He, C. Schneider, B. Ai, G. Wang, Z. Zhong, D. A. Dupleich, R. S. Thomae, M. Boban, J. Luo, and Y. Zhang, "Propagation channels of 5G millimeter-wave vehicle-to-vehicle communications: Recent advances and future challenges," *IEEE Veh. Technol. Mag.*, vol. 15, no. 1, pp. 16–26, Mar. 2020, doi: 10.1109/MVT.2019.2928898.

[4] M. Charitos and G. Kalivas, "MIMO HetNet IEEE 802.11p–LTE deployment in a vehicular urban environment," *Veh. Commun.*, vol. 9, pp. 222–232, Jul. 2017, doi: 10.1016/j.vehcom.2016.12.004.

[5] M. A. Karabulut, A. F. M. S. Shah, and H. Ilhan, "A novel MIMO-OFDM based MAC protocol for VANETs," *IEEE Trans. Intell. Transport. Syst.*, vol. 23, no. 11, pp. 20255–20267, Nov. 2022, doi: 10.1109/TITS.2022.3180697.

[6] P. Kumari, J. Choi, N. González-Prelcic, and R. W. Heath, "IEEE 802.11ad-based radar: An approach to joint vehicular communication-radar system," *IEEE Trans. Veh. Technol.*, vol. 67, no. 4, pp. 3012–3027, Apr. 2018, doi: 10.1109/TVT.2017.2774762.

[7] O. Sokunbi, H. Attia, A. Hamza, A. Shamim, Y. Yu, and A. A. Kishk, "New self-isolated wideband MIMO antenna system for 5G mm-wave applications using slot characteristics," *IEEE Open J. Antennas Propag.*, vol. 4, pp. 81–90, 2023, doi: 10.1109/OJAP.2023.3234341.

[8] P. Shariff B. G., A. A. Naik, T. Ali, P. R. Mane, R. M. David, S. Pathan, and J. Anguera, "High-isolation wide-band four-element MIMO antenna covering Ka-band for 5G wireless applications," *IEEE Access*, vol. 11, pp. 123030–123046, 2023, doi: 10.1109/ACCESS.2023.3328777.

[9] K. Cuneray, N. Akcam, T. Okan, and G. O. Arican, "28/38 GHz dual-band MIMO antenna with wideband and high gain properties for 5G applications," *Int. J. Electron. Commun.*, vol. 162, Apr. 2023, Art. no. 154553, doi: 10.1016/j.aeue.2023.154553.

[10] T. Abbas, J. Karedal, and F. Tufvesson, "Measurement-based analysis: The effect of complementary antennas and diversity on vehicle-to-vehicle communication," *IEEE Antennas Wireless Propag. Lett.*, vol. 12, pp. 309–312, 2013, doi: 10.1109/LAWP.2013.2250243.

[11] M. V. Rao, B. T. P. Madhav, J. Krishna, Y. U. Devi, T. Anilkumar, and B. Prudhvi Nadh, "CSRR-loaded T-shaped MIMO antenna for 5G cellular networks and vehicular communications," *Int. J. RF Microwave Comput.-Aided Eng.*, vol. 29, no. 8, pp. 1–19, Aug. 2019, doi: 10.1002/mmce.21799.

[12] U. Y. U. Devi, M. T. P. Boddapati, and T. A. Kumar, K. Skc, and P. Pardhasaradhi, "Conformal printed MIMO antenna with DGS for millimetre wave communication applications," *Int. J. Electron. Lett.*, vol. 8, no. 3, pp. 329–343, Jul. 2020, doi: 10.1080/21681724.2019.1600731.

[13] M. Ikram, K. S. Sultan, A. M. Abbosh, and N. Nguyen-Trong, "Sub-6 GHz and mm-wave 5G vehicle-to-everything (5G-V2X) MIMO antenna array," *IEEE Access*, vol. 10, pp. 49688–49695, 2022, doi: 10.1109/ACCESS.2022.3172931.

[14] N. Hussain and N. Kim, "Integrated microwave and mm-wave MIMO antenna module with 360° pattern diversity for 5G Internet of Things," *IEEE Internet Things J.*, vol. 9, no. 24, pp. 24777–24789, Dec. 2022, doi: 10.1109/JIOT.2022.3194676.

[15] P. S. Bhadrvathi Ghouse, P. R. Mane, S. Thankappan Sumangala, V. Kumar Puttur, S. Pathan, V. K. Jhunjhunwala, and T. Ali, "A compact dual-band millimeter wave antenna for smartwatch and IoT applications with link budget estimation," *Sensors*, vol. 24, no. 1, p. 103, Dec. 2023, doi: 10.3390/s24010103.

[16] C. Wang, E. Li, and D. F. Sievenpiper, "Surface-wave coupling and antenna properties in two dimensions," *IEEE Trans. Antennas Propag.*, vol. 65, no. 10, pp. 5052–5060, Oct. 2017, doi: 10.1109/TAP.2017.2738030.

[17] A. R. Sabek, W. A. E. Ali, and A. A. Ibrahim, "Minimally coupled two-element MIMO antenna with dual band (28/38 GHz) for 5G wireless communications," *J. Infr., Millim., Terahertz Waves*, vol. 43, nos. 3–4, pp. 335–348, Mar. 2022, doi: 10.1007/s10762-022-00857-3.

[18] K. D. Ayinala and P. K. Sahu, "Isolation enhanced compact dual-band quad-element MIMO antenna with simple parasitic decoupling elements," *Int. J. Electron. Commun.*, vol. 142, Dec. 2021, Art. no. 154013, doi: 10.1016/j.aeue.2021.154013.

[19] A. Iqbal, A. Smida, A. J. Alazemi, M. I. Waly, N. K. Mallat, and S. Kim, "Wideband circularly polarized MIMO antenna for high data wearable biotelemetric devices," *IEEE Access*, vol. 8, pp. 17935–17944, 2020, doi: 10.1109/ACCESS.2020.2967397.

[20] Y. Liu, X. Yang, Y. Jia, and Y. J. Guo, "A low correlation and mutual coupling MIMO antenna," *IEEE Access*, vol. 7, pp. 127384–127392, 2019, doi: 10.1109/ACCESS.2019.2939270.

[21] Q. Rubani, S. H. Gupta, and A. Rajawat, "A compact MIMO antenna for WBAN operating at terahertz frequency," *Optik*, vol. 207, Apr. 2020, Art. no. 164447, doi: 10.1016/j.ijleo.2020.164447.

[22] A. K. Singh, A. K. Dwivedi, C. Jha, S. Singh, V. Singh, and R. S. Yadav, "A compact MIMO antenna for 5G NR frequency bands n257/n258/n261 under millimeter-wave communication," *IETE J. Res.*, vol. 69, no. 12, pp. 8561–8573, Jun. 2022, doi: 10.1080/03772063.2022.2091044.

[23] Y. Jia, P. Xu, and X. Guo, "MIMO system capacity based on different numbers of antennas," *Results Eng.*, vol. 15, Sep. 2022, Art. no. 100577, doi: 10.1016/j.rineng.2022.100577.

[24] R. Ahmad, D. Pratap Singh, and M. Singh, "Ergodic capacity of MIMO channel in multipath fading environment," *Int. J. Inf. Eng. Electron. Bus.*, vol. 5, no. 3, pp. 41–48, Sep. 2013, doi: 10.5815/ijieeb.2013.03.05.

[25] K. Klionovski and A. Shamim, "Back radiation suppression through a semitransparent ground plane for a millimeter-wave patch antenna," *IEEE Trans. Antennas Propag.*, vol. 65, no. 8, pp. 3935–3941, Aug. 2017, doi: 10.1109/TAP.2017.2717967.

[26] S. Chen, J. Hu, Y. Shi, Y. Peng, J. Fang, R. Zhao, and L. Zhao, "Vehicle-to-everything (V2X) services supported by LTE-based systems and 5G," *IEEE Commun. Standards Mag.*, vol. 1, no. 2, pp. 70–76, Jul. 2017, doi: 10.1109/MCOMSTD.2017.1700015.

[27] A. I. Sulyman, A. T. Nassar, M. K. Samimi, G. R. Maccartney, T. S. Rappaport, and A. Alsanie, "Radio propagation path loss models for 5G cellular networks in the 28 GHZ and 38 GHZ millimeter-wave bands," *IEEE Commun. Mag.*, vol. 52, no. 9, pp. 78–86, Sep. 2014, doi: 10.1109/MCOM.2014.6894456.

[28] A. I. Sulyman, A. Alwarafy, G. R. MacCartney, T. S. Rappaport, and A. Alsanie, "Directional radio propagation path loss models for millimeter-wave wireless networks in the 28-, 60-, and 73-GHz bands," *IEEE Trans. Wireless Commun.*, vol. 15, no. 10, pp. 6939–6947, Oct. 2016, doi: 10.1109/TWC.2016.2594067.

[29] S. Sun, G. R. MacCartney, and T. S. Rappaport, "Millimeter-wave distance-dependent large-scale propagation measurements and path loss models for outdoor and indoor 5G systems," in *Proc. 10th Eur. Conf. Antennas Propag. (EuCAP)*. Switzerland: IEEE, Apr. 2016, pp. 1–5, doi: 10.1109/EUCAP.2016.7481506.

[30] M. N. Hindia, A. M. Al-Samman, T. A. Rahman, and T. M. Yazdani, "Outdoor large-scale path loss characterization in an urban environment at 26, 28, 36, and 38 GHz," *Phys. Commun.*, vol. 27, pp. 150–160, Apr. 2018, doi: 10.1016/j.phycom.2018.02.011.

[31] R. Schneider, D. Didascalou, and W. Wiesbeck, "Impact of road surfaces on millimeter-wave propagation," *IEEE Trans. Veh. Technol.*, vol. 49, no. 4, pp. 1314–1320, Jul. 2000, doi: 10.1109/25.875249.

[32] I. A. Hemadeh, K. Satyanarayana, M. El-Hajjar, and L. Hanzo, "Millimeter-wave communications: Physical channel models, design considerations, antenna constructions, and link-budget," *IEEE Commun. Surveys Tuts.*, vol. 20, no. 2, pp. 870–913, 2nd Quart., 2018, doi: 10.1109/COMST.2017.2783541.

[33] A. Iqbal, M. Al-Hasan, I. B. Mabrouk, and M. Nedil, "Scalp-implantable MIMO antenna for high-data-rate head implants," *IEEE Antennas Wireless Propag. Lett.*, vol. 20, pp. 2529–2533, 2021, doi: 10.1109/LAWP.2021.3117345.

[34] C. J. Ma, B. J. Xiang, S. Y. Zheng, and Y. M. Pan, "A miniaturized planar multibeam antenna for millimeter-wave vehicular communication," *IEEE Trans. Veh. Technol.*, vol. 72, no. 3, pp. 3611–3621, Mar. 2023, doi: 10.1109/TVT.2022.3220242.

[35] T. Nitsche, C. Cordeiro, A. B. Flores, E. W. Knightly, E. Perahia, and J. C. Widmer, "IEEE 802.11ad: Directional 60 GHz communication for multi-gigabit-per-second Wi-fi [Invited Paper]," *IEEE Commun. Mag.*, vol. 52, no. 12, pp. 132–141, Dec. 2014, doi: 10.1109/MCOM.2014.6979964.

[36] Z. Qamar, N. Aboserwal, and J. L. Salazar-Cerreno, "An accurate method for designing, characterizing, and testing a multi-layer radome for mm-wave applications," *IEEE Access*, vol. 8, pp. 23041–23053, 2020, doi: 10.1109/ACCESS.2020.2970544.

[37] Y. He and G. V. Eleftheriades, "A thin double-mesh metamaterial radome for wide-angle and broadband applications at millimeter-wave frequencies," *IEEE Trans. Antennas Propag.*, vol. 68, no. 3, pp. 2176–2185, Mar. 2020, doi: 10.1109/TAP.2019.2951491.

[38] M. Md. S. Hossain, S. A. N. Saqueb, A. H. Arage, J. Cabigao, C. Velasquez, K. Sertel, and N. K. Nahar, "Wideband radomes for millimeter-wave automotive radars," *IEEE Trans. Antennas Propag.*, vol. 70, no. 2, pp. 1178–1186, Feb. 2022, doi: 10.1109/TAP.2021.3118832.

[39] J. Wang, X. Zhao, Y. Ye, and S. Liu, "A millimeter-wave ultrawideband tightly coupled dipole array antenna for vehicle communication," *IEEE Antennas Wireless Propag. Lett.*, vol. 21, pp. 2135–2139, 2022, doi: 10.1109/LAWP.2022.3193438.

[40] K. Chen, J. Xu, Q. Lin, Y. Zhu, and W. Hong, "Single-layer wideband tilted beam phased array antenna for millimeter-wave vehicle communications," *IEEE Trans. Veh. Technol.*, vol. 73, no. 3, pp. 3536–3550, Mar. 2024, doi: 10.1109/TVT.2023.3323965.

[41] I. Mavromatis, A. Tassi, G. Rigazzi, R. J. Piechocki, and A. Nix, "Multi-radio 5G architecture for connected and autonomous vehicles: Application and design insights," 2018, *arXiv:1801.09510*.

[42] M. A. Abbas, A. Allam, A. Gaafar, H. M. Elhennawy, and M. F. A. Sree, "Compact UWB MIMO antenna for 5G millimeter-wave applications," *Sensors*, vol. 23, no. 5, p. 2702, Mar. 2023, doi: 10.3390/s23052702.

[43] M. E. Munir, S. H. Kiani, H. S. Savci, M. Marey, J. Khan, H. Mostafa, and N. O. Parchin, "A four element mm-wave MIMO antenna system with wide-band and high isolation characteristics for 5G applications," *Micromachines*, vol. 14, no. 4, p. 776, Mar. 2023, doi: 10.3390/mi14040776.

[44] B. Aghoutane, S. Das, M. E. Ghzaoui, B. T. P. Madhav, and H. E. Faylali, "A novel dual band high gain 4-port millimeter wave MIMO antenna array for 28/37 GHz 5G applications," *Int. J. Electron. Commun.*, vol. 145, Feb. 2022, Art. no. 154071, doi: 10.1016/j.aeue.2021.154071.

[45] M. I. Khan, S. Liu, M. K. Khan, and S. U. Rahman, "Eight elements mm-wave MIMO antenna for anti-collision radar sensing application with novel hybrid techniques," *Int. J. Electron. Commun.*, vol. 167, Jul. 2023, Art. no. 154687, doi: 10.1016/j.aeue.2023.154687.

[46] P. Tiwari, V. Gahlaut, M. Kaushik, A. Shastri, G. Siddiqui, and B. Singh, "A high-frequency planar-configured millimeter-wave MIMO antenna for fifth-generation NR operations," *Int. J. RF Microwave Comput.-Aided Eng.*, vol. 2023, pp. 1–14, Sep. 2023, doi: 10.1155/2023/9533725.

[47] Z. Chen, Y.-X. Wang, K.-D. Hong, and T. Yuan, "A multiantenna system with high isolations for millimeter-wave sensing," *IEEE Antennas Wireless Propag. Lett.*, vol. 21, pp. 2482–2486, 2022, doi: 10.1109/LAWP.2022.3198091.

B. G. PARVEEZ SHARIFF (Graduate Student Member, IEEE) received the B.E. degree in telecommunication engineering and the M.Tech. degree in digital electronics and communication systems from Visvesvaraya Technological University, Belagavi, India, in 2007 and 2009, respectively. He is currently pursuing the Ph.D. degree with the Electronics and Communication Engineering Department, Manipal Institute of Technology, Manipal, India. His research interests include microstrip antenna, array antenna, flexible antenna, and metamaterial structure. He is a Life Member of ISTE, India.

TANWEER ALI (Senior Member, IEEE) is currently an Associate Professor with the Department of Electronics and Communication Engineering, Manipal Institute of Technology, Manipal Academy of Higher Education, Manipal. He is an Active Researcher in the field of microstrip antennas, wireless communication, and microwave imaging. He has published more than 130 papers in reputed web of science (SCI) and Scopus indexed journals and conferences. He has led seven Indian patents, of which three have been published. He is on the board of reviewer of journals, such as IEEE TRANSACTIONS ON ANTENNAS AND PROPAGATION, IEEE ANTENNAS AND WIRELESS PROPAGATION LETTERS, IEEE ACCESS, and many other journals. He has been listed in top 2% scientists across the world for the year 2021 and 2022 by the prestigious list published by Stanford University, USA, indexed by Scopus.

PRAVEEN KUMAR received the B.E. degree in electronics and communication engineering and the M.Tech. degree in microelectronics and control systems from Visvesvaraya Technological University, Belagavi, Karnataka, India. He is currently pursuing the Ph.D. degree with Manipal Institute of Technology, Manipal Academy of Higher Education, Manipal, India. His research interest includes microstrip antennas. He is a member of IETE, India.

SAMEENA PATHAN is currently an Assistant Professor with the Department of Information and Communication Technology, Manipal Institute of Technology, Manipal Academy of Higher Education, Manipal. Her research interests include pattern recognition, medical image analysis, artificial intelligence, and machine learning.

G. D. GOUTHAM SIMHA received the Ph.D. degree from the National Institute of Technology Karnataka (NITK), Surathkal, India, in 2018. He was an Intern with LEOs ISRO Bangalore for the project entitled ''Design and implementation of ATP sensor for optical inter-satellite links,'' in 2008. He was a part of ''Uncoordinated Secure and Energy Aware Access in Distributed Wireless Networks'' project which was sponsored by the Information Technology Research Academy (ITRA), Media Laboratory Asia, in 2015. He was a Faculty Member with the Department of Electronics and Communication Engineering, NITK, Surathkal, from 2018 January to June 2019. He is currently an Associate Professor with the Department of Electronics and Communication Engineering, Manipal Institute of Technology, Manipal, Karnataka, India. His research interests include spatial modulation, RIS communications, massive MIMO, optical wireless communications, and error control coding.

PALLAVI R. MANE (Senior Member, IEEE) received the B.E. degree in electronics and communication engineering from the Gogte Institute of Technology, India, in 1996, the M.Tech. degree in digital electronics and advanced communication from the National Institute of Technology, Surathkal, Karnataka, India, in 2002, and the Ph.D. degree in electronics and communication engineering from Manipal Institute of Technology (MIT), MAHE, Manipal, for the thesis in network coding, in 2014. She is currently a Professor with the Department of ECE, MIT, MAHE. She has authored several papers in international conferences and journal proceedings. Her research interests include network coding, source, and channel coding, and communication engineering.

MOHAMMED GULAM NABI ALSATH (Senior Member, IEEE) received the B.E. and M.E. degrees from the College of Engineering, Anna University, Chennai, and the Ph.D. degree from Anna University for his research work on automotive antennas. He is currently an Associate Professor with the Department of Electronics and Communication Engineering, College of Engineering Guindy, Anna University. His research interests include microwave components and circuits, antenna engineering, signal integrity analysis, and solutions to EMI problems.

ALEXANDROS-APOSTOLOS A. BOULOGEORGOS (Senior Member, IEEE) was born in Trikala, Greece, in 1988. He received the Diploma degree in electrical and computer engineering (ECE) and the Ph.D. degree in wireless communications from the Aristotle University of Thessaloniki (AUTH), in 2012 and 2016, respectively. From October 2012 to September 2016, he was a Teaching Assistant with the Department of ECE, AUTH. From February 2017 to September 2022, he was an Adjunct Professor with the Department of ECE, University of Western Macedonia, Greece, and as a Visiting Lecturer with the Department of Computer Science and Biomedical Informatics, University of Thessaly. From 2017 to 2022, he was a Senior Researcher with the Department of Digital Systems, University of Piraeus, where he conducted research in the area of wireless communications. Since 2022, he has been an Assistant Professor with the Department Electrical and Computer Engineering, University of Western Macedonia. He has worked in a number of EU and national projects. He has (co-)authored more than 140 technical papers, which were published in scientific journals and presented at prestigious international conferences. He is the holder of two (one national and one European) patents, while he has filled other three patents.